Chemical Engineering Journal 523 (2025) 167723

Contents lists available at ScienceDirect

Chemical Engineering Journal

journal homepage: www.elsevier.com/locate/cej

Glycerol oxi-dehydration to acrylic acid experimental assessment: Effect of catalyst properties, reaction parameters, and bed configurations

Yash Bansod [a,*], Prashant Pawanipagar [a], Umar Abubakar [a], Min Hu [a,*], Hassan Alhassawi [a], Kamran Ghasemzadeh [a], Luke Forster [a], Sarayute Chansai [a], Christopher Hardacre [a], Vincenzo Spallina [a,*], Carmine D'Agostino [a,b,**]

[a] *Department of Chemical Engineering, University of Manchester, Manchester M13 9PL, UK*
[b] *Dipartimento di Ingegneria Civile, Chimica, Ambientale e dei Materiali (DICAM), Alma Mater Studiorum – Università di Bologna, Via Terracini, 28, 40131 Bologna, Italy*

ARTICLE INFO

Keywords:
Glycerol
Acrylic acid
Oxi-dehydration
Zeolite
Molybdenum-vanadium oxide
Reactor configuration

ABSTRACT

This study presents the proof-of-principle and sensitivity analysis of a dual-bed catalytic system achieving exceptional acrylic acid yield (up to 67.2 %) from glycerol oxi-dehydration - among the highest reported in the literature. A systematic investigation was carried out to boost the catalytic performance by investigating several variables, including type of catalysts, reaction parameters, and bed configurations. The reaction process involved the dehydration of glycerol to acrolein over HZSM-5 zeolites, followed by further oxidation to acrylic acid using vanadium-molybdenum mixed oxide catalysts having orthogonal (Ortho-MoVO) or amorphous structure (Amor-MoVO). HZSM-5 zeolites with Si/Al ratios ranging from 23 to 500 were evaluated in the presence and absence of air at 280 °C for the glycerol dehydration, with HZSM-5 (200) showing optimal performance. The dual-bed configuration (HZSM-5/MoVO) significantly outperformed the mixed-bed system, with Amor-MoVO achieving the highest yield of 67.2 % at 280 °C. When using Ortho-MoVO under optimized conditions (280 °C, 4972 h^{-1} GHSV, oxygen-to-glycerol ratio of 9.5), the system maintained a high acrylic acid yield of 58.8 %. The superior performance of the dual-bed system was attributed to the spatial separation of reaction zones, enabling controlled oxygen exposure and minimizing undesired oxidation pathways. The main by-products from the oxi-dehydration reaction in the dual-bed system were acetic acid, propanoic acid, formic acid and CO_x, however, additional by-products such as acetaldehyde, propanal and acrolein were observed in the case of the mixed-bed system. This study demonstrates the feasibility of a promising route for the sustainable acrylic acid production from renewable feedstocks, with a perspective on industrial implementation.

1. Introduction

The growing environmental concerns due to anthropogenic activities, particularly the excessive utilization of fossil fuels and the consequent increase in greenhouse gas emissions, have highlighted the importance of producing chemicals from renewable biomass sources. Biodiesel, derived from renewable biomass, has emerged as an excellent alternative to fossil fuels, promising to alleviate environmental pressure and promote sustainable development. Hence, a significant rise in biodiesel production has been seen over the last two decades [1]. As a result, glycerol, a byproduct of biodiesel production, has become increasingly abundant [2,3]. This glycerol can be converted to value-added products, such as acrolein by dehydration; lactic acid by oxidation; syngas by reforming; solketal by acetalization; propanediol by hydrogenolysis; esters by esterification; ether by etherification and glycerol carbonate by oxidative carbonylation [4]. Among these, the dehydration reaction of glycerol to acrolein has been particularly attractive as it offers a green and sustainable alternative to the current non-renewable method of acrolein production from propylene [5].

Acrolein is an important chemical in the modern chemical industry. It is an intermediate for producing acrylic acid along with various other important chemicals such as DL-methionine, glutaraldehyde, 1,2,6-hexanetriol, quinoline, and pentaerythritol. [6,7]. Various catalysts such as

---

[*] Corresponding authors.
[**] Correspondence to: C. D'Agostino, Department of Chemical Engineering, University of Manchester, Manchester M13 9PL, UK.

E-mail addresses: yash.bansod@postgrad.manchester.ac.uk (Y. Bansod), min.hu@manchester.ac.uk (M. Hu), vincenzo.spallina@manchester.ac.uk (V. Spallina), carmine.dagostino@manchester.ac.uk (C. D'Agostino).

https://doi.org/10.1016/j.cej.2025.167723
Received 25 November 2024; Received in revised form 20 August 2025; Accepted 24 August 2025

Abbreviations

HZSM-5	Zeolite Socony Mobil-5 (protonated form)
Ortho-MoVO	Orthorhombic Molybdenum-Vanadium Oxide
Amor-MoVO	Amorphous Molybdenum-Vanadium Oxide
GHSV	Gas Hourly Space Velocity
COx	Carbon Oxides (CO and CO2)
XRD	X-ray Diffraction
FTIR	Fourier Transform Infrared Spectroscopy
DRIFTS	Diffuse Reflectance Infrared Fourier Transform Spectroscopy
SEM	Scanning Electron Microscopy
EDX	Energy Dispersive X-ray Spectroscopy
BET	Brunauer-Emmett-Teller
TPD	Temperature Programmed Desorption
TGA	Thermogravimetric Analysis
XRF	X-Ray Fluorescence
TCD	Thermal Conductivity Detector
NH_3	Ammonia
Si/Al	Silicon to Aluminium ratio
CEM	Controlled Evaporator Mixture

Symbols

λ	Wavelength (Å)
θ	Diffraction angle
z_i	Number of carbon atoms
T	Temperature (°C)
ΔH^0	Standard enthalpy change
I	Intensity
I_0	Initial intensity
ID	Inner Diameter
L	Length

heteropoly acids [8,9], zeolites [10,11], metal oxides [12,13], and phosphate catalysts were found to be active and selective for acrolein production through gas-phase glycerol dehydration in the literature. Zeolites have emerged as favourable catalysts for the gas-phase dehydration of glycerol due to their distinct advantages such as high surface area, tuneable acidity, good hydrothermal stability and commercial availability at a relatively cheaper price [14]. Many researchers have reported that the appropriate amount of Brønsted acid sites plays a crucial role in achieving high acrolein selectivity. The number of Brønsted acid sites is dependent on the Si/Al ratio of the zeolite framework with a higher ratio generally leading to a lower number of acid sites [10].

HZSM-5 zeolites have been reported as good candidates for the dehydration reaction. However, despite the advantageous catalytic properties for the gas-phase dehydration of glycerol, low selectivity towards acrolein is typically observed at high glycerol conversion, and the catalysts often suffer from low stability due to coke formation. Coke formation can occur through two distinct pathways: polyglycols formed on the external surface via intermolecular dehydration of glycerol at adjacent sites, followed by consecutive coupling of hydroxyl groups, and polyaromatics formed inside the pores, potentially originating from unsaturated oxygen heterocycles produced from various intermediates and reaction products [15–17]. The formation of these coke precursors can also result from acrolein, which can undergo further reactions such as hydride transfer, cracking, isomerization, aldol condensation, Diels-Alder reactions, dehydrogenation, and/or hydrogenation, leading to the formation of aldehydes, olefins, heterocyclic, and aromatic compounds with high molecular weight [18]. To circumvent these issues, a subsequent conversion of acrolein to a more stable and desirable product, immediately after its formation, would not only enhance the selectivity towards the target product but also eliminate the challenges associated with acrolein handling, such as storage and transportation.

$$C_3H_8O_3 \rightarrow C_3H_4O + 2H_2O \Delta H^0 = 12.46\frac{kJ}{mol_{C_3H_8O_3}} \tag{1}$$

$$C_3H_4O + \frac{1}{2}O_2 \rightarrow C_3H_4O_2 \Delta H^0 = -254.1\frac{kJ}{mol_{C_3H_4O}} \tag{2}$$

One major industrial application of acrolein is the production of acrylic acid, an important industrial chemical for a variety of commodity products such as superabsorbent polymer production, acrylic fibres, detergents, surface coatings, textiles, and adhesives [19]. Typical oxidation catalysts for this process involve vanadium-molybdenum mixed oxides due to their high selectivity towards acrylic acid [20,21], with reaction parameters such as gas hourly space velocity (GHSV), temperature and oxygen partial pressure playing crucial roles in catalyst performance. Recent research efforts have focused on the development of catalyst systems to improve selectivity and yield in the direct conversion of glycerol to acrylic acid. Several studies have explored various dehydration and oxidation catalysts with changing reaction parameters, with promising results. For instance, Witsuthammakul et al. [15] reported 40 % acrylic acid yield with HZSM-5 as the dehydration catalyst and 79 wt% molybdenum 21 wt% vanadium supported on silicic acid as the oxidation catalyst. However, in this work, vanadium-molybdenum mixed oxides were prepared hydrothermally rather than by conventional support impregnation methods. These hydrothermally synthesized catalysts are known to provide excellent performance for acrolein oxidation to acrylic acid (Eq. (2)) with yield as high as 93 % due to their unique crystal structure and enhanced metal-oxygen interaction [21].

In this work, the dehydration of glycerol to acrolein was investigated using HZSM-5 zeolites (with Si/Al ratios ranging from 23 to 500) to identify the best catalyst for this first reaction step (Eq. (1)) of the overall acrylic acid manufacturing process starting from glycerol as feedstock. Subsequently, the conversion (oxi-dehydration) of glycerol to acrylic acid was studied using the best dehydration catalyst in combination with the hydrothermally prepared vanadium-molybdenum mixed oxides as the oxidation catalyst. This strategic pairing of optimized catalysts, combined with a systematic investigation of bed configurations and reaction parameters (GHSV, temperature, glycerol to oxygen ratio), was designed to achieve superior control over the complete reaction pathway from glycerol to acrylic acid. The comprehensive analysis and approach targeted both individual reaction steps and their integration, overcoming the limitations of previous fragmented studies to maximize the yield of acrylic acid.

2. Methodology

2.1. Materials and chemicals

HZSM-5 with different Si/Al ratios (23, 30, 80, 200–400, 400–570) were obtained commercially from Thermo Scientific. Ammonium molybdate tetrahydrate (Fisher Scientific) and vanadium oxide sulphate hydrate (97.0 %, Sigma-Aldrich) were used as the metal precursor for the oxidation catalysts (Ortho-MoVO and Amor-MoVO), whereas oxalic acid was purchased from Aldrich. Glycerol (>99.5 %) used in the reaction was purchased from Thermo Scientific. Silicon carbide pellets (F-24 Mesh Coarse) were purchased from Clear Minerals.

2.2. Catalyst preparation

The zeolites were calcined at 550 °C for 6 h and then the zeolite powder was pressed into a dense disc using a hydraulic press at 7 bar for

15 min. The resulting disc was crushed using a mechanical grinder and sieved through standard meshes (750 μm and 550 μm) to obtain particles in the 550–750 μm size range before using them in the reaction. MoVO oxide catalyst was synthesized via a hydrothermal method [21]. An aqueous solution of ammonium molybdate (8.82 g in 120 mL deionized water) was prepared, and to this, an aqueous solution of vanadyl oxide sulphate (3.28 g in 120 mL deionized water) was added dropwise at ambient temperature under continuous stirring. The resulting mixed solution was stirred for an additional 10 min and then transferred to an autoclave equipped with a Teflon inner tube. The concentration of Mo in the final solution was 0.2 mol/L whereas for V, it was 0.05 mol/*L*. Prior to the hydrothermal reaction, N_2 gas was purged into the solution inside the tube to remove residual oxygen in the mixture. The hydrothermal reaction was conducted at 175 °C for 48 h in an electric oven. After the reaction, the formed grey solid product was separated by filtration, washed with distilled water, and dried overnight in air at 80 °C. The catalysts obtained after this process were orthorhombic phase of MoVO oxide (Ortho-MoVO). To prepare amorphous phase MoVO oxide (Amor-MoVO), the concentration of the starting solutions was doubled, and the N_2 gas purging step was omitted from the process.

2.3. Catalyst characterization

The powder XRD data of all the catalysts were collected on a Panaytical X'Pert Pro Diffractometer which was equipped with a Copper Line Focus X-ray tube with Nickel kβ absorber (λ = 1.542 Å). The powder XRD data were collected with a step size of 0.03°. FTIR Spectra presented were recorded with a Bruker Vertex 70 Fourier-Transform Infrared Spectrometer and 256 scans were taken with 4 cm^{-1} resolution. Raman spectra were recorded on a Horiba JY LabRAM HR 800 Raman spectrometer coupled with microscope in reflectance mode with 633 nm excitation laser sources and a spectral resolution of 0.3 cm^{-1}. Energy dispersive X-ray fluorescence spectrometer (EDXRF, PANalytical MiniPal 4) was used to determine the elements in the catalysts. SEM-EDX analysis of the catalysts was performed on a FEI Quanta 250 system and the samples were coated with a 10 nm layer of Au/Pd coating to prevent charging.

Thermogravimetric analysis (TGA) was performed on both fresh and spent catalysts using a Shimadzu TGA-50 instrument. Samples were subjected to a linear temperature ramp from 20 °C to 900 °C at a rate of 10 °C min^{-1} under an air flow of 40 mL min^{-1}. Temperature-programmed desorption of ammonia (NH_3-TPD) was conducted using a BELCAT II Catalyst Analyzer equipped with a thermal conductivity detector (TCD). For the initial pretreatment, the sample was heated from ambient temperature to 350 °C at a rate of 10 °C min^{-1} under 40 mL min^{-1} He flow. The sample was then allowed to cool till it reached 40 °C followed by NH_3 adsorption. For NH_3 adsorption, a mixture of 10 % of NH_3 in Argon was flowed through the sample for 30 min at 40 °C. Physically adsorbed NH_3 was removed by flowing Ar at 40 °C for 30 min. Finally, the sample was heated to 800 °C at 10 °C min^{-1} for 45 min while measuring NH_3 with TCD data which was analysed by MicrotracBEL Corp ChemMasterII. Using the same BELCAT II analyzer, temperature-programmed reduction (H_2-TPR) measurements were also performed. The MoVO oxide samples (50–60 mg) were initially outgassed at 200 °C for 1 h under He flow (20 mL min^{-1}) and subsequently cooled to room temperature. The samples were then heated to 700 °C under a 10 % H_2/Ar gas mixture (20 mL min^{-1}) at a heating rate of 5 °C min^{-1}, while monitoring the hydrogen consumption using the TCD detector.

Nitrogen adsorption-desorption isotherms were obtained using a Micromeritics ASAP 2060 physisorption analyzer. Prior to analysis, approximately 150 mg of sample was degassed at 300 °C under vacuum (0.5 mmHg) for 4 h. The physisorption measurements were conducted at −196 °C (77 K). The Brunauer-Emmett-Teller (BET) method was employed to determine the specific surface area, while the t-plot method was used to calculate the pore volume of the materials.

In-situ Diffuse Reflectance Infrared Fourier Transform Spectroscopy (DRIFTS) measurements were conducted using a Bruker Vertex 70 FTIR spectrometer equipped with a liquid N_2-cooled mercury-cadmium-telluride detector. A ceramic crucible containing approximately 20 mg of the catalyst sample was placed in the DRIFTS cell. The catalyst was pre-treated to remove moisture by heating in argon (Ar) at a total flow rate of 50 cm^3 min^{-1} to 300 °C for 1 h, followed by cooling to 25 °C under Ar flow. The IR spectrum of the catalyst at 25 °C under flowing Ar was recorded as a background. Pyridine adsorption was performed at 30 °C using pyridine vapor generated from a saturator with Ar as a carrier gas. The pyridine saturator was maintained in an ice bath to achieve a pyridine concentration of 2000 ppm. The total flow rate was maintained at 50 cm^3 min^{-1}. After 30 min of exposure, the weakly adsorbed pyridine was purged from the catalyst surface for 10 min using Ar. In-situ DRIFTS spectra were recorded with a resolution of 4 cm^{-1}, accumulating 128 scans every 60 s during transient switches. Spectral analysis was performed using OPUS software. IR data are reported as log 1/R ('absorbance'), where $R = I/I_0$, I is the intensity measured under reaction conditions, and I_0 is the intensity measured on the pure catalyst powder under Ar flow at 25 °C.

2.4. Catalytic experiments

The reaction was conducted in a tubular stainless reactor (ID = 10 mm, L = 30 cm) located in an electrical furnace (as shown in Fig. 1). For dehydration reactions, 1 g of zeolites (HZSM-5) mixed with 4 g of silicon carbide pellets were packed as a single bed catalyst. The length of the catalyst zone inside the reactor after filling it with dehydration catalyst was 4.1 cm. For oxi-dehydration reactions and dual bed configuration, 1 g of oxidation catalyst (MoVO oxide) mixed with 4 g of silicon carbide pellets was packed under the zeolite bed for subsequent oxidation testing whereas in case of mixed bed system both the dehydration and oxidation catalysts were mixed together physically before loading into the reactor. The length of the catalyst zone inside the reactor after filling it with both the catalysts was 7.8 cm. Detailed schematics of how the mixed and dual bed configurations were packed are shown in Fig. 2. He, N_2 and air were regulated using mass flow controllers. The catalysts were activated at 300 °C for 1 h with N_2 flowing. Then, the temperature was adjusted to the reaction temperature (260–300 °C) and held for 30 min before the reaction. Glycerol solution (10 wt%) was then fed using a liquid flow controller and the mixture was evaporated in a controlled evaporator mixture (CEM) before flowing it to the reactor. The reaction was carried out for 7 h time on stream. The product effluents were trapped by a cooling condenser (<3 °C) and collected hourly. The liquid products were quantitatively analyzed by gas chromatography with a thermal conductivity detector (GC–TCD). A capillary SH-Wax Crossbond carbowax polyethylene glycol (Shimadzu; ID = 0.25 mm, L = 30 m, df = 0.25 μm) was used as separating column. For the gaseous products, gas chromatography equipped with thermal conductivity detector (GC–TCD) and a molecular sieve 13× (1/8 in × 8 ft) column. Eqs. (3), (4) and (5) used to calculate glycerol conversion, product yield and product selectivity are mentioned below.

$$\text{Glycerol conversion} = \frac{\text{moles of glycerol}(C_3H_8O_3)\text{ reacted}}{\text{moles of glycerol}(C_3H_8O_3)\text{ fed}} \times 100 \tag{3}$$

$$\text{Product selectivity} = \frac{\text{moles of product formed}}{\text{moles of glycerol}(C_3H_8O_3)\text{ reacted}} \times \frac{z_i}{3} \times 100 \tag{4}$$

$$\text{Product yield} = \frac{\text{moles of product formed}}{\text{moles of glycerol}(C_3H_8O_3)\text{ fed}} \times \frac{z_i}{3} \times 100 \tag{5}$$

where z_i represents the number of carbon atoms of the respective product *i* to discriminate the product distribution against the carbon conversion of the original feedstock.

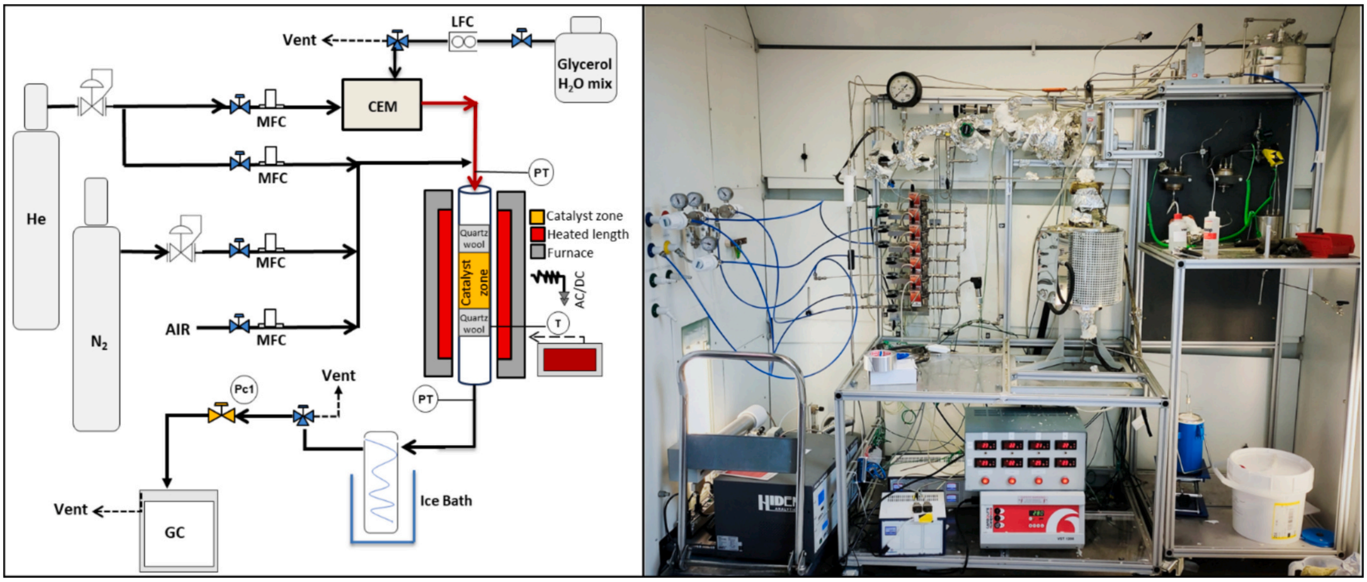

Fig. 1. Schematic of the experimental setup (left) and actual experimental setup (right).

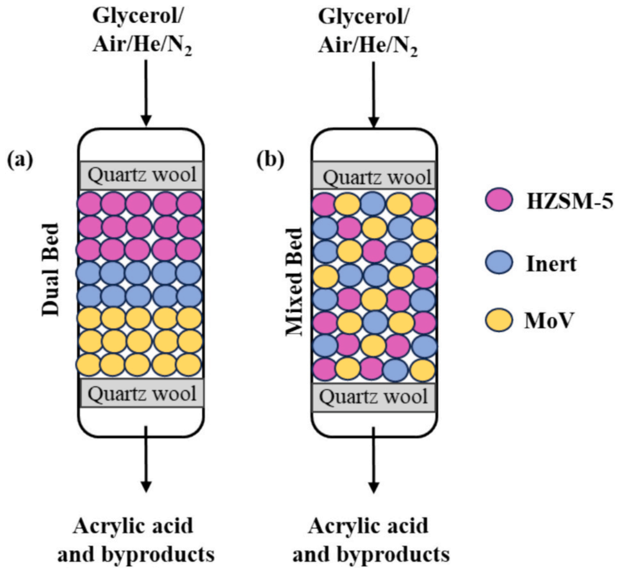

Fig. 2. Schematic of (a) dual bed and (b) mixed bed configurations used in experimental study.

Carbon balance (Eq. (6)) was calculated as the sum of residual glycerol (C_{Gly}) and total detected products in the liquid (C_{liquid}) and gas (C_{gas}) phases. For the dehydration reactions, observed carbon balances did not achieve 100 % but was limited to (80–90 %), attributable to several factors: (1) presence of minor and high-molecular-weight products at unquantifiable concentrations, (2) potential thermal decomposition of some products during chromatographic analysis, and (3) possible incomplete recovery of volatile components in the condensation apparatus. In Eq. (7), N_i denotes the number of moles of compound *i*.

$$\text{Carbon balance} = C_{Gly} + C_{liquid} + C_{gas} \tag{6}$$

$$\begin{aligned} 3N_{gly,in} = {} & 3N_{gly,out} + N_{CO} + N_{CO_2,} + 2N_{acetaldehyde} + 3N_{acetone} + 3N_{propanal} \\ & + 3N_{acrolein} + 3N_{hydroxyacetone} + 3N_{propane\ diol} + 2N_{acetic\ acid} \\ & + 3N_{propanoic\ acid} + N_{formic\ acid} + 3N_{acrylic\ acid} \end{aligned} \tag{7}$$

The oxi-dehydration of glycerol to acrylic acid is influenced by multiple factors, each playing a crucial role in determining the efficiency and selectivity of the reaction. In this work, four key parameters: temperature (260 to 300 °C), GHSV (553 h^{-1} to 4977 h^{-1}), oxygen-to-glycerol ratio (4.7–14.2), and catalyst bed configuration were investigated with each parameter varied independently while maintaining standard operating conditions for all other variables to isolate and understand its specific effect on acrylic acid yield. In general, temperature affects reaction kinetics and thermodynamics, potentially shifting the balance between desired products and unwanted side reactions. Moreover, the dehydration of glycerol to acrolein (Eq. (1)) is slightly endothermic, whereas the subsequent oxidation of acrolein to acrylic acid (Eq. (2)) is highly exothermic. GHSV impacts the residence time of reactants and intermediates, influencing the extent of reaction and product distribution. Oxygen concentration is critical in balancing the oxidation steps while minimizing over-oxidation [22]. In addition, oxygen is essential for efficient acrolein oxidation to acrylic acid while avoiding the formation of undesired CO_x products (CO and CO_2). Finally, the catalyst bed configuration - either mixed-bed or dual-bed – determined the reaction pathway and the degree of control over each step of the process. By examining these effects in detail, valuable insights can be drawn to operate the glycerol oxi-dehydration process for maximum acrylic acid yield and selectivity.

3. Results and discussion

3.1. Physical and chemical characteristics of the catalysts

X-ray diffraction (XRD) patterns of the zeolite samples are presented in Fig. 3(a). The region of 2θ between 5° and 35° reveals characteristic MFI diffraction planes (101), (200), (051), (033), and (313), corresponding to diffraction peaks at approximately 8.01°, 8.90°, 23.10°,

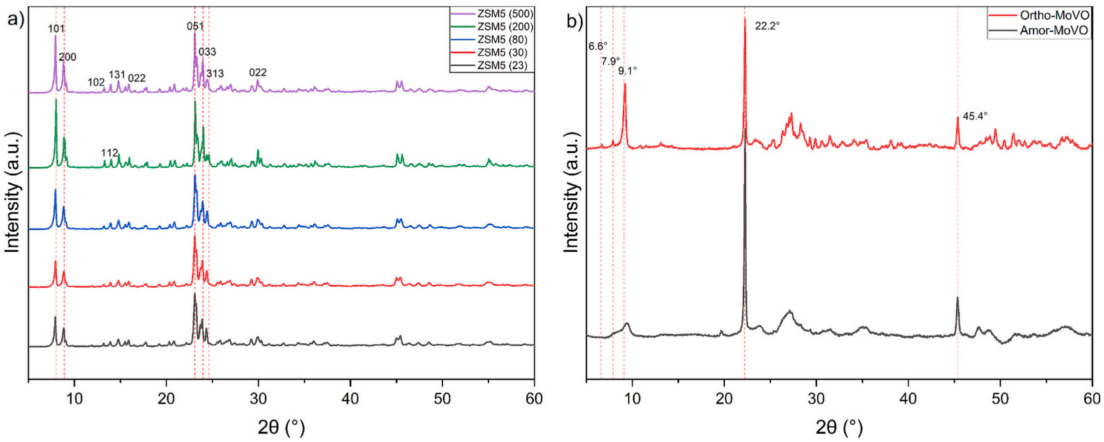

Fig. 3. X-ray diffraction patterns of a) HZSM-5 (23), HZSM-5 (30), HZSM-5 (80), HZSM-5 (200) and HZSM-5 (500), b) Ortho-MoVO and Amor-MoVO.

Table 1
Properties of the HZSM-5 catalysts.

Dehydration catalyst

Catalyst	Crystallite size (nm)	Composition (Si/Al)	Surface area (m^2/g)	Pore volume (cm^3/g)		Acidity (mmol/g)			
				Micropore volume	Mesopore volume	Total	Weak	Strong	B/L ratio
HZSM-5 (23)	23	10.8	330.10	0.128	0.067	1.835	1.220	0.517	1.90
HZSM-5 (30)	22	13.4	320.57	0.113	0.084	1.42	1.001	0.315	2.11
HZSM-5 (80)	21	48.3	375.65	0.122	0.111	0.809	0.527	0.150	0.83
HZSM-5 (200)	21	170.8	384.64	0.056	0.165	0.235	0.152	0.043	0.17
HZSM-5 (500)	22	261.1	363.35	0.069	0.131	0.208	0.194	0.007	0.08

Oxidation catalyst

Catalyst	Crystallite size (nm)	Composition (Mo/V)	Surface area (m^2/g)	Pore volume (cm^3/g)	H_2 uptake (mmol/g)
Ortho-MoVO	34	3.10	11.80	0.017	2.562
Amor-MoVO	29	3.03	5.11	0.009	2.167

23.98°, and 24.61°, respectively [23]. The XRD diffractograms showed no phases other than HZSM-5, confirming the purity and crystallinity of the samples. Crystallite sizes calculated using the Scherrer equation [24], ranged from 21 to 23 nm for all zeolites, while Ortho-MoVO and Amor-MoVO exhibited larger crystallite sizes of 34 nm and 29 nm, respectively (Table 1). X-ray fluorescence (XRF) analysis revealed that both MoVO materials primarily consisted of Mo (Ortho-MoVO: 83.66 %, Amor-MoVO: 81.94 %) and V (Ortho-MoVO: 14.32 %, Amor-MoVO: 14.35 %), with a Mo/V molar ratio of 3.10 and 3.03, respectively, which was also observed by Chen et al. [21] by ICP-AES analysis. Fig. 3 (b) illustrates the crystalline structures of the two MoVO materials. Both patterns display one strong diffraction peak at 22.2° and a weaker peak at 45.4°, indicating a shared layered-type structure [21]. In addition to these peaks, the Ortho-MoVO catalyst also showed three its characteristic diffraction peaks (6.6°, 7.9°, and 9.0°) at angle lower than 10° [25]. Considering a three-dimensional crystal lattice with mutually perpendicular x, y, and z axes in an orthogonal coordinate system, Ortho-MoVO demonstrated good crystallinity along all axes, exhibiting characteristic

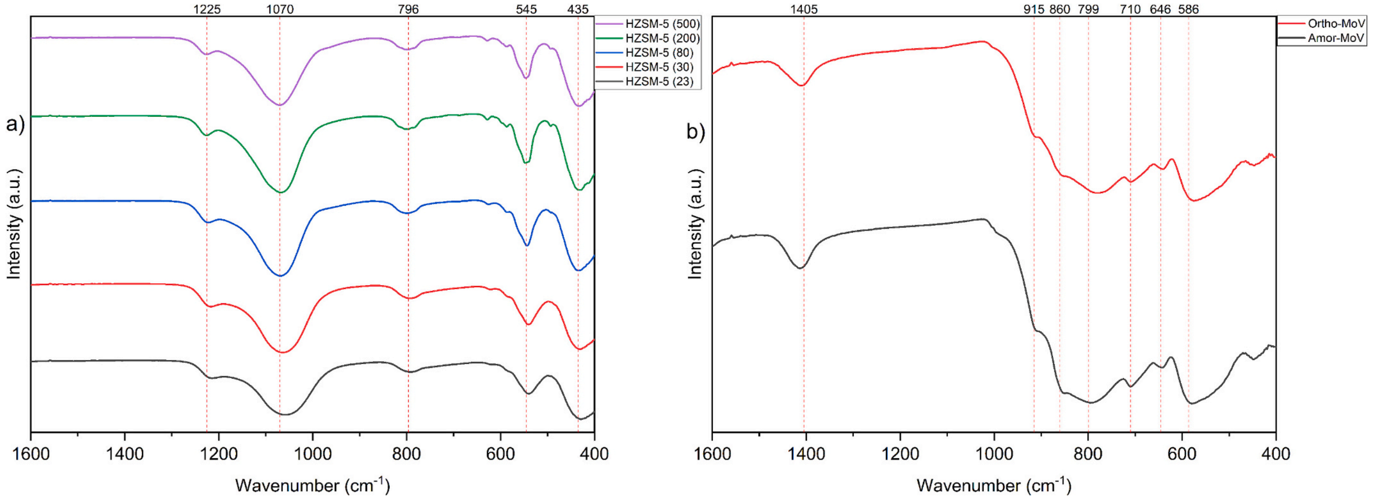

Fig. 4. FTIR spectra of a) HZSM-5 (23), HZSM-5 (30), HZSM-5 (80), HZSM-5 (200) and HZSM-5 (500), b) Ortho-MoVO and Amor-MoVO.

diffraction peaks of an orthorhombic system. In contrast, Amor-MoVO lacked well-defined crystallinity in the xy plane, suggesting an amorphous structure [21].

FTIR spectroscopy was employed to characterize the zeolite framework vibrations and silanol groups (Fig. 4(a)). The spectra reveal characteristic absorption bands at 1225 cm^{-1} (external asymmetric stretch), ~1070 cm^{-1} (internal asymmetric stretch), 796 cm^{-1} (external symmetric stretch), and 435 cm^{-1} (T-O bend), typical of siliceous materials [26,27]. A band at 545 cm^{-1}, characteristic of the double five rings in MFI-type zeolites, serves as an indicator of crystallinity [28]. The high intensity of this band in HZSM-5 (200) suggests a high degree of crystallinity, as also confirmed by the XRD results. FTIR spectra of the synthesized MoVO samples (Fig. 4(b)) provide insights into their structural characteristics. The absorption at 860 cm^{-1} is attributed to symmetric stretching vibrations of Mo═O cis-dioxo groups, while bands at 799, 710, and 646 cm^{-1} correspond to antisymmetric vibrations of Mo—O—X (X = Mo, V) bridging bonds [29,30]. Additional bands at 915 and 586 cm^{-1} are associated with V═O groups and V—O—X (X = Mo) bonds, respectively [31]. The presence of these metal-oxygen bond-related absorption bands in both MoVO samples indicates a consistent basic structure of the metal oxide framework, despite the differences in crystallinity observed in XRD analysis.

SEM images of the zeolite samples (Fig. 5) reveal a correlation between increasing Si/Al ratio and the particle morphology. As the Si/Al ratio increases, catalyst particles tend to adopt a more spherical shape, accompanied by a reduction in agglomeration. All zeolite samples exhibit homogeneous particle shapes, with no other morphologies observed. EDX analysis confirmed that the estimated Si/Al ratios closely match the values provided by the commercial zeolite suppliers (Table 1).

For the MoVO catalysts (Fig. 5), both Ortho-MoVO and Amor-MoVO display rod-shaped morphologies, as evidenced in the SEM micrographs. These rod-like structures vary in length, with an average diameter ranging from 0.2 to 0.4 μm. This distinct morphology contrasts with the more spherical particles observed in the high Si/Al ratio zeolites, potentially influencing the catalytic performance in the dehydration of glycerol.

Nitrogen adsorption-desorption isotherms of the zeolite samples exhibit a combination of Type I and Type IV profiles, indicating the presence of both narrow micropores and mesopores [32]. This dual porosity characteristic is further supported by the pore volume distribution data presented in Table 1. Notably, the isotherms for HZSM-5 (23), HZSM-5 (30), and HZSM-5 (80) display a Type H4 hysteresis loop (Fig. S1, SI), which is typically associated with aggregated zeolite crystals. This observation aligns with the morphological features observed in the SEM analysis, further confirming the aggregated nature of these samples. BET surface area measurements were conducted to facilitate comparison with literature values. The surface areas obtained in this study are consistent with previously reported values for similar HZSM-5 materials, validating the textural properties of catalysts used in this study [33]. The combination of micropores and mesopores in these zeolite catalysts plays a crucial role in the dehydration of glycerol, potentially influencing reactant diffusion and product selectivity. The presence of mesopores, in particular, could enhance the accessibility of active sites and facilitate the transport of larger molecules involved in the reaction pathway.

The acidic properties of the zeolite catalysts were investigated using temperature-programmed desorption of ammonia (NH_3-TPD). NH_3-TPD profiles (Fig. 6(a)) reveal two distinct desorption peaks for the zeolite samples. The low-temperature peak (~200 °C) corresponds to weak acidic sites, while the high-temperature peak (>350 °C) is attributed to strong acidic sites [34]. Quantitative analysis of the acidic sites (Table 1) demonstrates a clear trend: the number of strong acidic sites decreases with increasing Si/Al ratio [35]. Notably, HZSM-5 (500) exhibits negligible strong acid sites, indicating a significant change in acid site distribution at high Si/Al ratios.

While NH_3-TPD provides valuable information on acid site strength and quantity, it cannot distinguish between Brønsted and Lewis acid sites. To address this limitation, DRIFTS analysis using pyridine as a probe molecule was performed (Fig. 6(b)). The spectra reveal characteristic peaks at 1445 cm^{-1} and 1614 cm^{-1}, attributed to Lewis acid sites [36]. A peak at 1597 cm^{-1} indicates H-bonded pyridine, while the peak at 1492 cm^{-1} represents a combination of Brønsted and Lewis acid sites [37]. Importantly, a peak at 1542 cm^{-1}, observed only in the HZSM-5 catalysts, is specifically associated with Brønsted acid sites. A notable trend emerges from the DRIFTS analysis: as the Si/Al ratio increases, the intensity of the Brønsted acid site peak (1542 cm^{-1}) diminishes, eventually disappearing in high Si/Al ratio HZSM-5 zeolites. Quantitatively, while HZSM-5 (23) shows the highest Brønsted acid peak area (2.87) compared to HZSM-5 (30) (1.78), it also exhibits a higher Lewis acid peak area (1.51 vs 0.84), resulting in a slightly lower B/L ratio of 1.90 compared to 2.11 for HZSM-5 (30). Beyond this, the B/L ratio decreases dramatically with increasing Si/Al ratio, falling to 0.83 for HZSM-5 (80), 0.17 for HZSM-5 (200), and ultimately 0.08 for HZSM-5 (500). This observation suggests a significant shift in the nature of acid sites with changing Si/Al ratios, which may have profound implications for the catalytic performance in the dehydration of glycerol to acrylic acid.

The complex interplay between catalyst properties and glycerol dehydration performance has been extensively studied in literature. Wang et al. [11] reported that acrolein formation was favoured by the cooperative action of Brønsted and Lewis acid sites in zeolites, highlighting the importance of maintaining a balance between different acid site types. Dalla Costa et al. [38] demonstrated that both total acidity

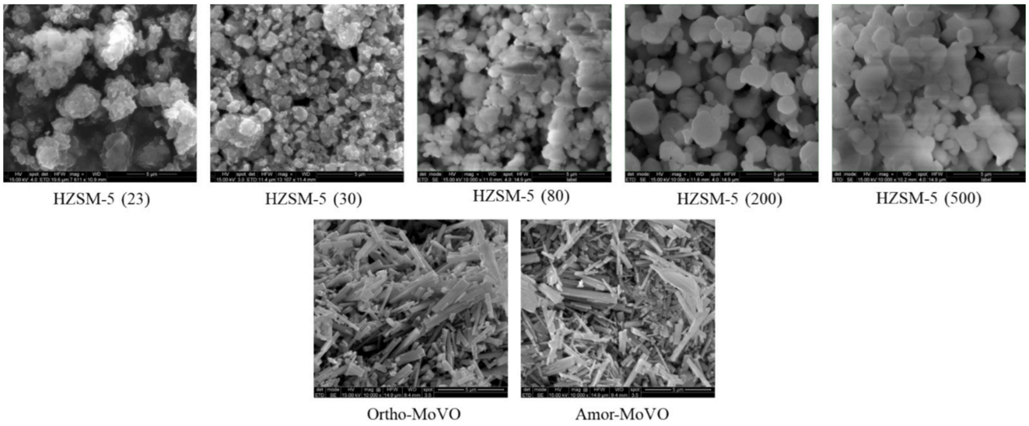
HZSM-5 (23) HZSM-5 (30) HZSM-5 (80) HZSM-5 (200) HZSM-5 (500)

Ortho-MoVO Amor-MoVO

Fig. 5. SEM images of dehydration catalysts (HZSM-5 (23), HZSM-5 (30), HZSM-5 (80), HZSM-5 (200) and HZSM-5 (500)) and oxidation catalysts (Ortho-MoVO and Amor-MoVO).

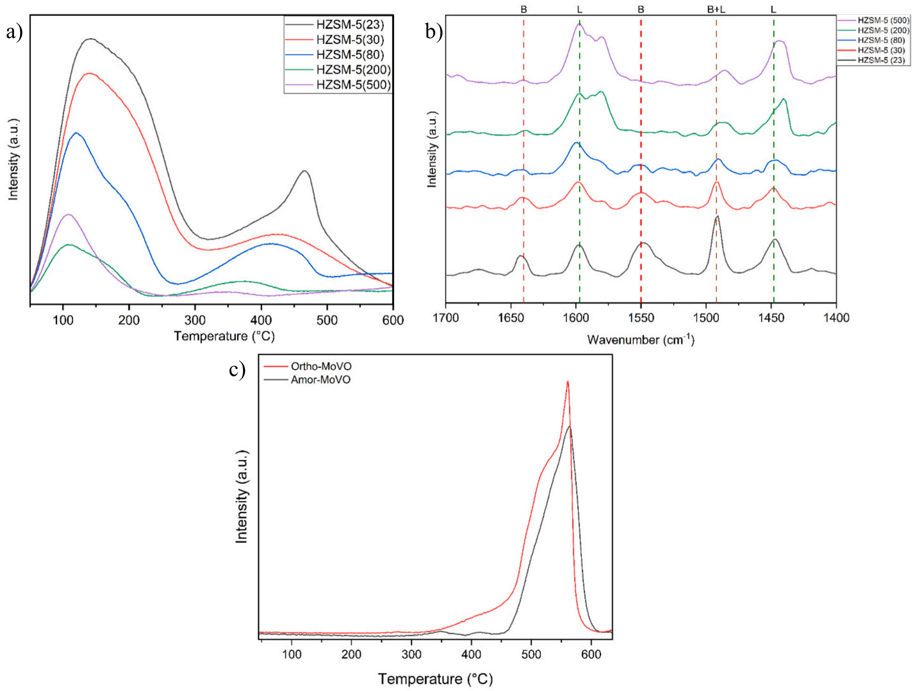

Fig. 6. a) Temperature-programmed desorption of ammonia (NH_3-TPD), b) DRIFTS spectra for HZSM-5 (23), HZSM-5 (30), HZSM-5 (80), HZSM-5 (200) and HZSM-5 (500), and c) temperature-programmed reduction by hydrogen (TPR-H_2) profiles for Ortho-MoVO and Amor-MoVO catalysts.

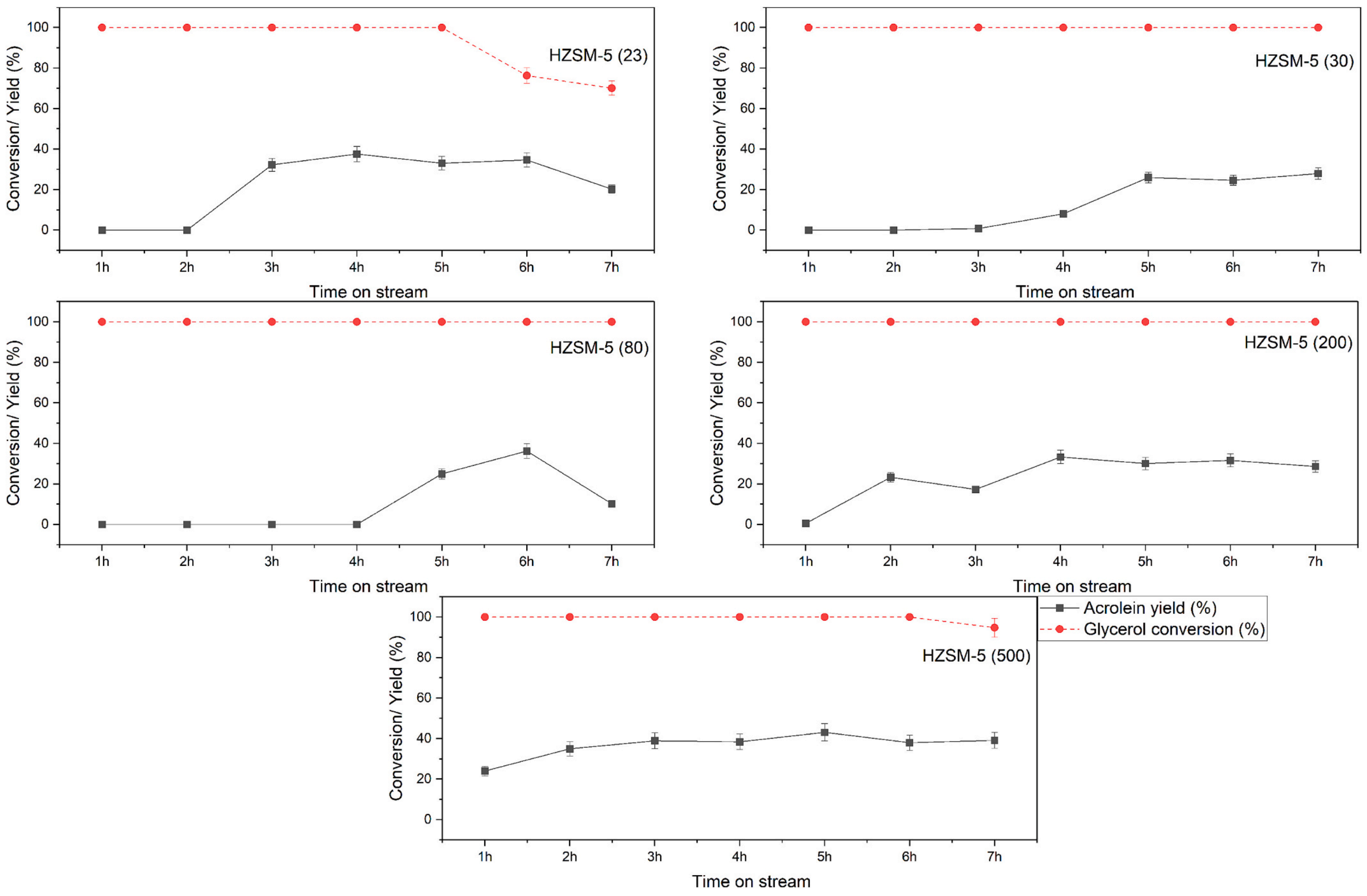

Fig. 7. Acrolein yield and glycerol conversion with time-on-stream over different HZSM-5 catalysts in absence of air. Reaction conditions: temperature= 280 °C; GHSV = 1412 h^{-1}; feed composition (mol%) glycerol/H_2O/N_2/He = 1.1/49.9/24.5/24.4.

and acid site strength distribution are crucial, with zeolites having a higher density of strong-medium strength sites exhibiting superior performance. Kim et al. [39] emphasized the role of pore structure, noting that while micropores were prone to carbon deposition, mesopores enhanced glycerol accessibility to active sites. In the context of our HZSM-5 catalysts with varying Si/Al ratios, optimal catalytic performance in glycerol dehydration likely requires high mesoporosity, a balanced distribution of Brønsted and Lewis acid sites, and an appropriate mix of weak and strong acidic sites. These structure-activity relationships provide valuable guidance for the rational design of zeolite catalysts for the dehydration of glycerol to acrylic acid via acrolein.

Fig. 6(c) shows the TPR profiles of Ortho-MoVO and Amor-MoVO. It can be seen that a prominent reduction peak centred around 550 °C is present for both samples, with Ortho-MoVO exhibiting a distinctive broader shoulder extending from approximately 400 °C. The quantitative analysis showed that Ortho-MoVO demonstrated a higher hydrogen uptake capacity of 2.562 mmol/g compared to 2.167 mmol/g for Amor-MoVO, indicating more reducible species in the orthorhombic structure. The main reduction peak can be attributed to the simultaneous reduction of Mo^{6+} to Mo^{4+} (and potentially to MoO) and V^{5+} species from the surface, while the broader shoulder observed in Ortho-MoVO suggests a more gradual reduction process or better-exposed active sites. The sharper reduction peak in Amor-MoVO indicates a more sudden, single-step reduction event.

3.2. Dehydration of glycerol to acrolein

The conversion of glycerol to acrylic acid via acrolein involved two steps: the initial dehydration of glycerol to acrolein, followed by the oxidation of acrolein to acrylic acid. Initial catalyst screening focused on five HZSM-5 zeolites with varying Si/Al ratios, evaluated over a 7 h period. These zeolites were tested both with and without air, considering their structural and acidic properties as crucial factors influencing catalytic activity.

As can be seen in Fig. 7, experimental results showed that HZSM-5 (30), (80), and (200) achieved complete glycerol conversion without air, while HZSM-5 (23) and (500) exhibited slightly lower conversion rates (79.0 % and 95.0 %, respectively) after 7 h. Gas chromatography analysis identified CO, CO_2, H_2, and CH_4 as gas-phase products, while liquid-phase products included acetaldehyde, propanal, acrolein, hydroxyacetone, acetic acid, propanoic acid, 1,2-propanediol, 1,3-propanediol, formic acid, and acrylic acid as shown in Table 2.

In the presence of air (Fig. 8), all catalysts except HZSM-5 (23) achieved 100 % conversion, indicating that air enhances the catalytic activity. Acrolein showed varying yields across different catalysts and conditions. In the absence of air, HZSM-5 (500) exhibited the highest acrolein yield (37.8 %), followed by HZSM-5 (200) at 30.1 %. Interestingly, in the presence of air, HZSM-5 (200) showed the highest acrolein yield (43.6 %). This shift suggested that the presence of air interacted with the catalyst surface as a cleaning mechanism for coke [40]. The distribution of by-products varied with both Si/Al ratio and the presence of air. Lower Si/Al ratio catalysts tended to produce more acetaldehyde and propanal, possibly due to their higher acidity promoting side reactions. Additionally, the formation of acrylic acid is observed only in the presence of air, which is sensible as oxygen plays a crucial role in the subsequent oxidation of acrolein to acrylic acid [22]. The high catalytic activity HZSM-5 (200) also correlated with its mesoporosity, which improved glycerol diffusion within the material [41]. Coke deposition was identified as a primary cause of catalyst deactivation by covering acid sites and blocking pores and cages, thus limiting access to active sites [42].

As shown in Fig. S2 (SI), thermogravimetric analysis (TGA) was employed to assess coke formation on HZSM-5 catalysts recovered after reaction done with and without air in the feed stream. Fresh catalyst samples showed weight loss primarily between 25 and 150 °C, attributed to moisture and physically adsorbed species release. Spent HZSM-5 samples exhibited two distinct weight loss regions: 150–350 °C (soft coke) and 350–750 °C (hard coke) [10,40]. Catalysts used in oxygen-free reaction conditions showed higher total weight loss compared to those used in reactions with air feed after 7 h of operation, with HZSM-5 (80) being an exception showing minimal difference between the two conditions. The total coke formation followed the order: HZSM-5 (23) $>$ HZSM-5 (30) $>$ HZSM-5 (80) $>$ HZSM-5 (500) $>$ HZSM-5 (200) under N_2 atmosphere, correlating with their micropore volume and acid site density. Hard coke constituted the majority of deposited coke and was partially removed in the presence of air for all zeolites (see Table S1 in the SI). The presence of air reduced hard coke formation by 35–60 % across all catalysts, demonstrating oxygen's effectiveness in continuous coke removal. HZSM-5 (200) and HZSM-5 (500) showed the lowest weight loss with air, likely due to their higher mesopore volume (0.165 cm^3/g and 0.131 cm^3/g, respectively) facilitating faster mass transfer and decreased coke deposition [10]. HZSM-5 (23) and HZSM-5 (30) had relatively higher coke deposition, possibly related to their larger micropore volume, which may favour coke precursor formation due to low reactant diffusion.

All HZSM-5 samples showed weight losses in both soft and hard coke regions, with hard coke losses being substantially higher. Soft coke formation showed less sensitivity to air presence, with reductions of only

Table 2
Conversion and selectivity over different HZSM-5 zeolites in glycerol dehydration reaction[c].

	In absence of air[a]					In presence of air[b]				
Catalyst	HZSM-5 (23)	HZSM-5 (30)	HZSM-5 (80)	HZSM-5 (200)	HZSM-5 (500)	HZSM-5 (23)	HZSM-5 (30)	HZSM-5 (80)	HZSM-5 (200)	HZSM-5 (500)
Conversion (%)	79.0	100.0	100.0	100.0	95.0	70.1	100.0	100.0	100.0	100.0
Molar selectivity (%)										
Acetaldehyde	0.9	2.3	3.3	1.4	2.0	0.5	8.3	5.0	7.7	7.1
Propanal	1.4	2.1	3.2	2.6	2.0	0.9	1.9	2.0	3.1	1.0
Acrolein	29.8	25.9	23.5	30.1	39.8	31.6	29.7	31.9	43.6	24.8
Hydroxyacetone	5.5	3.8	1.8	3.5	6.3	4.0	1.1	–	–	–
Acetic acid	0.8	0.9	1.6	2.3	0.2	0.3	2.3	2.7	2.1	3.0
Propanoic acid	0.3	1.7	5.9	1.0	0.4	1.9	3.8	4.5	3.5	0.4
1,3-Propane diol	0.5	0.4	0.3	0.0	1.3	1.0	0.4	0.4	0.3	0.3
Formic acid	0.0	–	–	–	0.1	–	1.1	0.6	1.3	7.1
Acrylic acid	–	–	0.4	0.4	–	–	2.9	1.6	3.5	0.8
CO_x	0.9	2.3	1.5	1.0	1.9	1.9	5.1	5.8	9.1	5.1

[a] Reaction conditions: 280 °C, 1 atm; Molar ratio: $Gly/H_2O/He/N_2 = 1.1/49.9/24.5/24.4$; GHSV $= 1565\ h^{-1}$.
[b] Reaction conditions: 280 °C, 1 atm; Molar ratio: $Gly/O_2/H_2O/He/N_2 = 1.1/5.1/49.9/24.5/19.3$; GHSV $= 1565\ h^{-1}$.
[c] Conversion and selectivity data were obtained as averages over the last 3 h of time-on-stream.

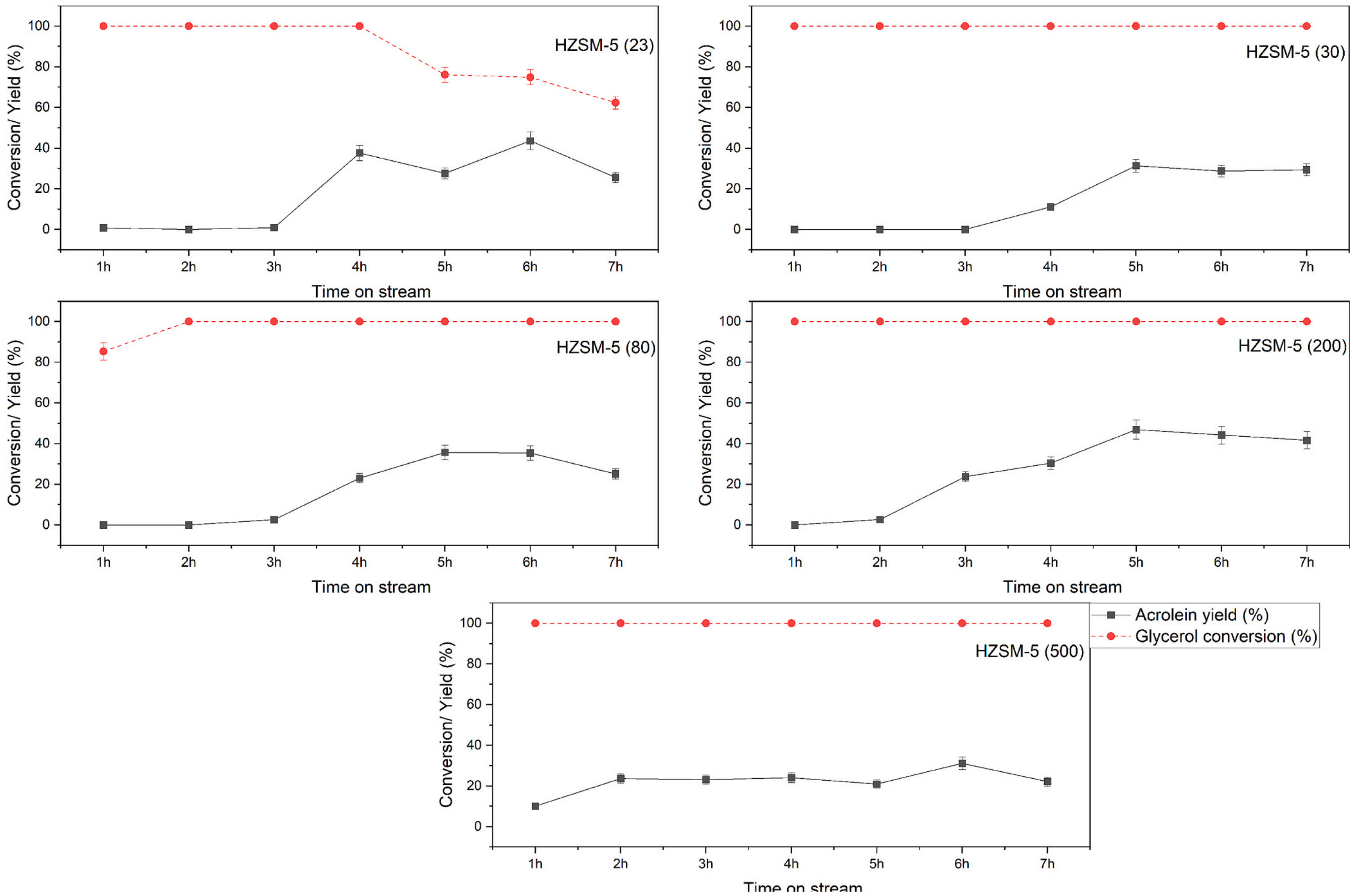

Fig. 8. Acrolein yield and glycerol conversion with time-on-stream over different HZSM-5 catalysts in presence of air. Reaction conditions: temperature = 280 °C; GHSV = 1412 h^{-1}; feed composition (mol%) Gly/O_2/H_2O/He/N_2 = 1.1/5.1/49.9/24.5/19.3.

10–25 %, while hard coke demonstrated dramatic decreases of 40–70 % when air was co-fed. For HZSM-5 (200), soft coke weight loss remained similar with and without air, while hard coke weight loss decreased from 4.9 % to 2 % with air. Notably, HZSM-5 (200) analysed after 14 h of catalytic testing at 280 °C with air showed comparable behaviour to the 7 h test under identical conditions, indicating a relatively constant rate of coke deposition and removal by air on the catalyst surface. TGA results were supported by increased CO and CO_2 production when oxygen was introduced, emphasizing oxygen's crucial role in maintaining catalyst surface cleanliness during reactions.

The mechanism shown in Fig. 9 illustrates two parallel pathways for glycerol conversion: (a) dehydration via Brønsted acid sites, where glycerol proceeds through a 3-hydroxypropanal intermediate to form acrolein, and (b) transformation over Lewis acid sites, which leads to hydroxyacetone formation. While previous research has predominantly focused on maximizing strong Brønsted acid sites to enhance acrolein production (as Lewis acid sites typically promote hydroxyacetone formation), our findings reveal that a balanced acidity profile yields superior results. This observation aligns with Wang et al. [11], who demonstrated that the cooperative interaction between Brønsted and Lewis acid sites can significantly enhance the selective formation of acrolein.

Considering both acrolein yield and potential for further conversion to acrylic acid, HZSM-5 (200) was selected as the optimal catalyst for the glycerol dehydration step in the two-step conversion of glycerol to acrylic acid. This zeolite achieved the highest acrolein selectivity (43.6 %) among tested catalysts and showed compatibility with oxidative conditions, evidenced by a notable acrylic acid yield (3.5 %) in the presence of air. This performance can be attributed to its balanced properties - high surface area, optimal mesopore volume, and moderate acidity - making it the most suitable candidate for integration with subsequent oxidation catalysts.

3.3. *Oxi-dehydration of glycerol to acrylic acid*

Fig. 10 shows the proposed reaction mechanism for acrolein oxidation to acrylic acid over the MoVO catalyst [43,44]. The efficiency of this oxidation step, along with the initial glycerol dehydration, is significantly influenced by various operational parameters. Understanding these effects is crucial for optimizing the overall process performance. Key variables including temperature, space velocity, oxygen concentration, and catalyst bed configuration were systematically investigated in the below sections to maximize acrylic acid yield while minimizing undesired side reactions.

3.3.1. *Effect of temperature*

The dual-bed system achieved its maximum acrylic acid yield of 58.8 % at 280 °C, followed by a significant decrease to 46.4 % at 300 °C as shown in Fig. 11 (also shown in Table S3 in the SI). This distinct temperature dependence reflected the advantage of spatially separated reaction zones. At 280 °C, both the dehydration and oxidation steps were seen to be near their optimal temperatures. The decrease at 300 °C might be due to accelerated side reactions or thermal decomposition of acrylic acid in the second bed. With respect to CO_x, the lower CO_x formation in the dual-bed system (24.3 % at 280 °C vs. 41.0 % in mixed-bed) suggested better control over complete oxidation, due to the staged reaction process and reduced catalyst interference. For the mixed-bed system, the increase in acrylic acid yield with temperature (30.4 % at 260 °C to 41.3

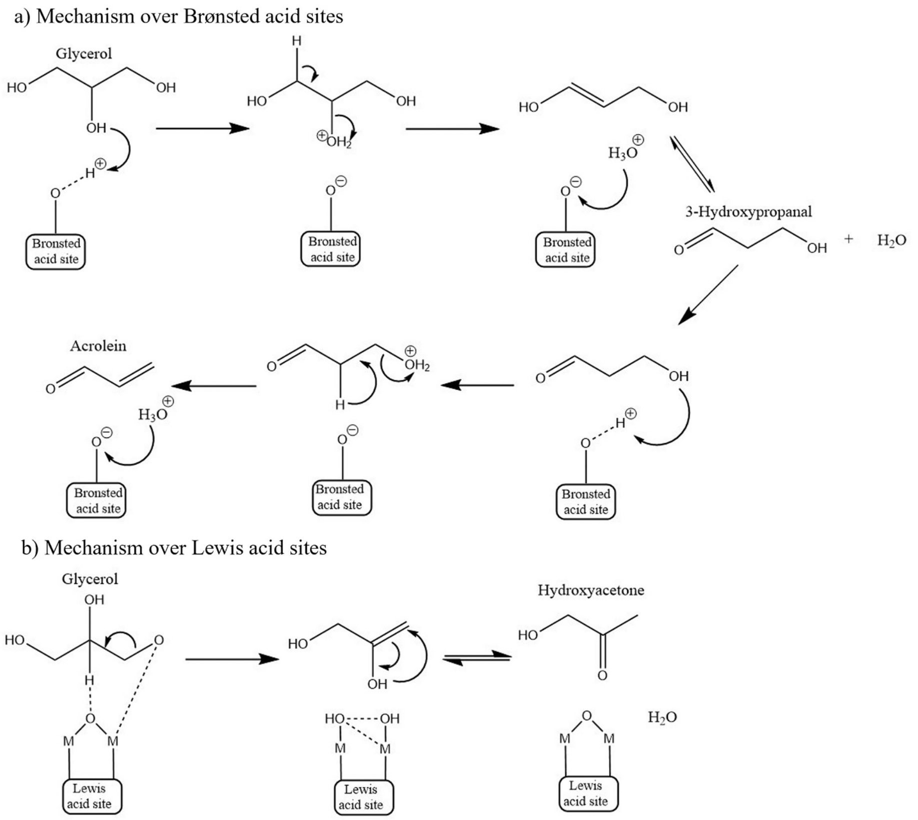

Fig. 9. Reaction mechanism of glycerol dehydration to acrolein over (a) Brønsted acid sites and (b) Lewis acid sites (b).

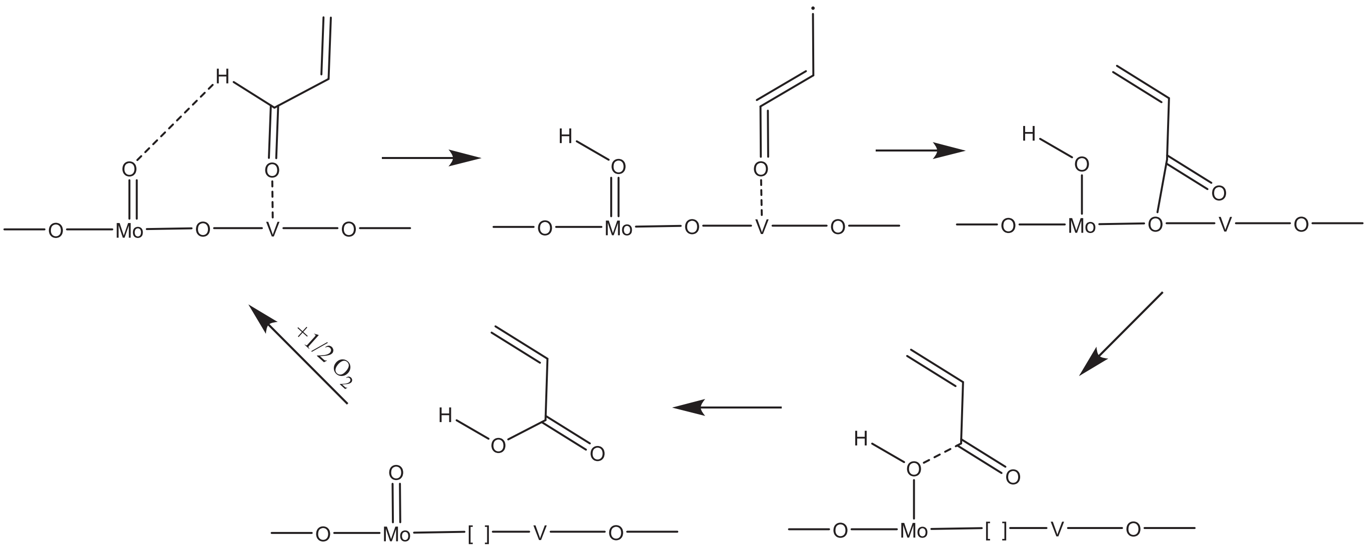

Fig. 10. Reaction mechanism for acrolein oxidation to acrylic acid over the MoVO catalyst surface proposed by Andrushkevich et al. [44] and Fjermestad et al. [43].

% at 300 °C) suggests a complex interplay of reactions. At higher temperatures, the dehydration of glycerol to acrolein likely accelerated on the HZSM-5 catalyst. Simultaneously, the oxidation of acrolein to acrylic acid on the MoVO catalyst was also enhanced as a significant jump was seen in the acrylic acid yield (31.6 % to 41.3 %) from 280 °C to 300 °C. However, this kinetic enhancement also promotes undesired complete oxidation pathways, as evidenced by increased CO_x formation rising from 33.1 % at 260 °C to 37.5 % at 300 °C. This suggested that while higher temperatures favour acrylic acid formation, they also promoted undesired complete oxidation reactions.

3.3.2. Effect of space velocity

Both the dual-bed and mixed-bed systems showed increased acrylic acid yield with higher GHSV, but the mechanisms involved might differ. For the dual-bed system, the remarkable increase in acrylic yield from 25.1 % to 58.8 % with increasing GHSV suggests that the separate beds allow for better performance of each step in terms of acrylic acid yield as shown in Fig. 12 (also shown in Table S4 in the SI). Higher space velocities might prevent acrolein decomposition in the first bed and reduce its residence time in the oxidation bed, minimizing over-oxidation. The lower CO_x formation in the dual-bed system across all GHSV values

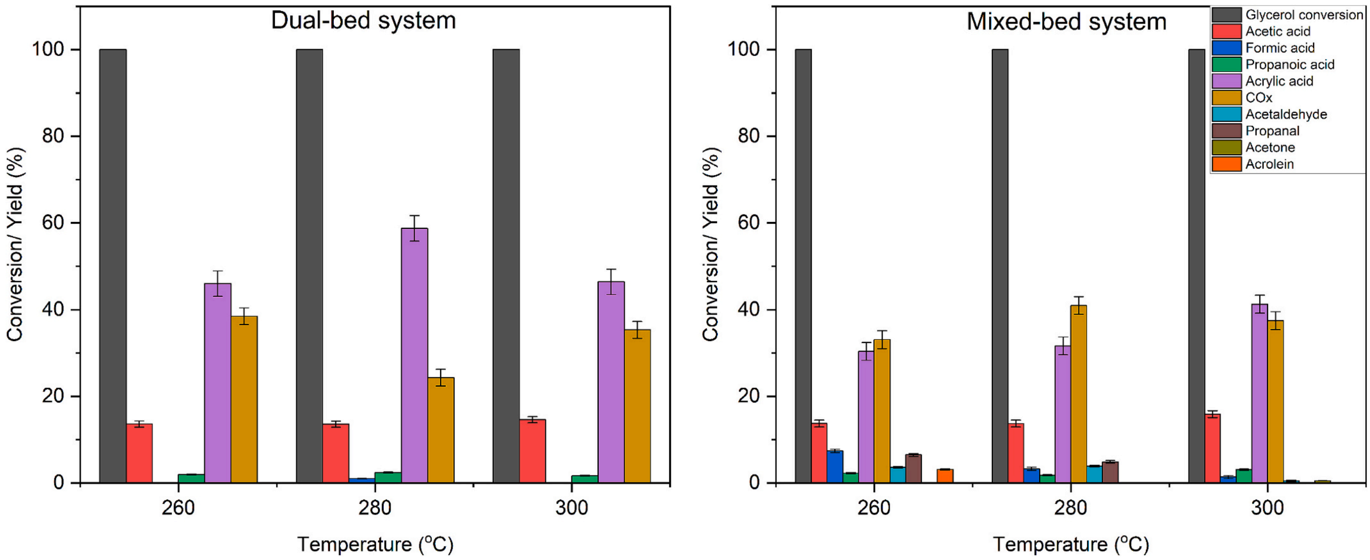

Fig. 11. Effect of temperature on the conversion and yield for glycerol oxi-dehydration to acrylic acid for dual and mixed-bed reactor system. Reaction conditions: dehydration catalyst was HZSM-5 (200) and oxidation catalyst was Ortho-MoVO; GHSV = 4978 h^{-1}; feed composition (mol%) glycerol/O_2/H_2O/N_2/He = 0.7/6.9/33.5/26.0/32.9. Conversion and yield data was taken after 3 h time-on-stream.

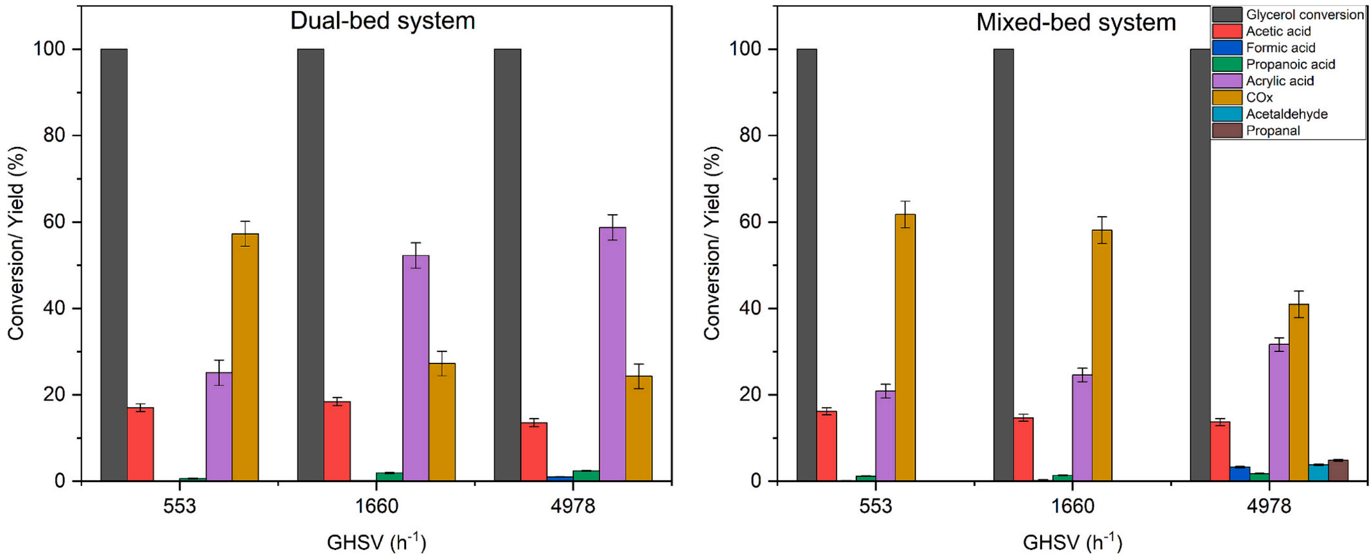

Fig. 12. Effect of gas hourly space velocity (GHSV) on the conversion and yield for glycerol oxi-dehydration to acrylic acid for dual and mixed-bed reactor system. Reaction conditions: dehydration catalyst was HZSM-5 (200) and oxidation catalyst was Ortho-MoVO; temperature = 280 °C; feed composition (mol%) glycerol/O_2/H_2O/N_2/He = 0.7/6.9/33.5/26.0/32.9. Conversion and yield data was taken after 3 h time-on-stream.

indicates better control over the oxidation process, due to the physical segregation of different reaction steps in the two beds. For the mixed bed, the yield increase from 20.9 % (553 h^{-1}) to 31.6 % (4977 h^{-1}) was due to reduced contact time preventing over-oxidation. This is supported by the decrease in CO_x yield from 61.7 % to 41.0 %. The presence of both catalysts in the same bed might cause rapid oxidation of intermediates at low GHSV, which is mitigated at higher velocities.

3.3.3. Effect of oxygen concentration

The dual-bed system demonstrated superior performance compared to mixed bed with an optimal acrylic acid yield of 58.8 % at an oxygen-to-glycerol ratio of 9.5. Moreover, the dual-bed configuration showed higher tolerance to oxygen variation, maintaining high acrylic acid yields (54.0–58.8 %) across all tested ratios as shown in Fig. 13 (also shown in Table S5 in the SI). This suggested that the separation of dehydration and oxidation steps allows for better oxygen utilization in the second bed. The consistent CO_x formation (24.3–26.0 %) across oxygen concentrations in the dual-bed system indicated better control over complete oxidation, possibly due to the targeted oxygen exposure to the catalyst in the second bed.

In contrast, the mixed-bed system showed higher sensitivity to oxygen concentration. The acrylic acid yield initially decreased from 39.5 % to 31.6 % as the oxygen-to-glycerol ratio decreased from 14.2 to 9.5, followed by a further decline to 29.4 % at 4.5. This progressive decline at lower oxygen concentrations coincided with increased formation of partial oxidation products: acetaldehyde (8.9 %), propanal (11.1 %), and acrolein (11.6 %). The presence of these intermediates indicates oxygen-limited conditions hindered complete conversion to acrylic acid. At the highest oxygen-to-glycerol ratio of 14.2, the maximum acrylic acid yield of 39.5 % was achieved, suggesting that higher oxygen availability favoured the selective oxidation pathway while maintaining moderate CO_x formation (39.3 %).

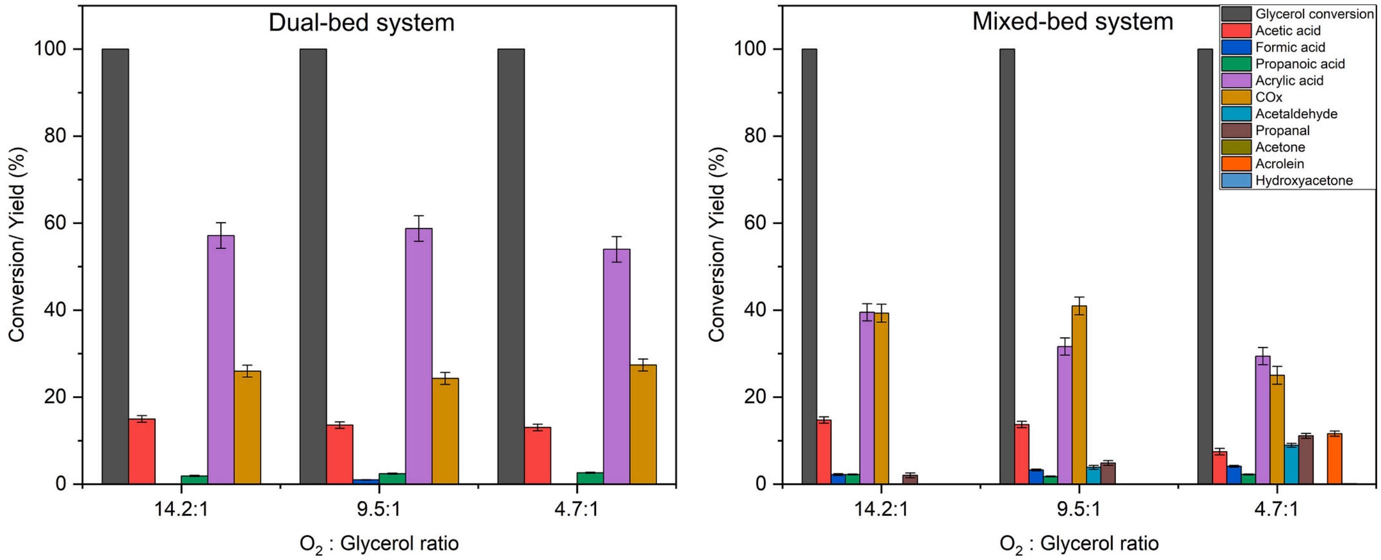

Fig. 13. Effect of oxygen-to-glycerol ratio on the conversion and yield for glycerol oxi-dehydration to acrylic acid for dual and mixed-bed reactor system. Reaction conditions: dehydration catalyst was HZSM-5 (200) and oxidation catalyst was Ortho-MoVO; temperature = 280 °C; GHSV = 4978 h^{-1}. Conversion and yield data was taken after 3 h time-on-stream.

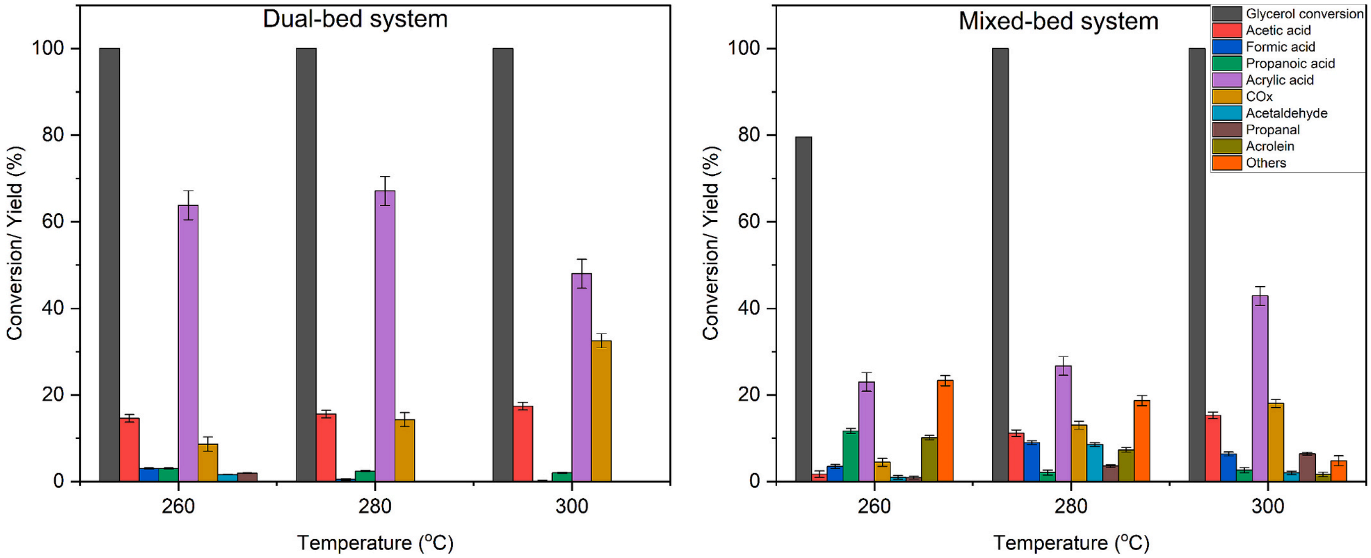

Fig. 14. Conversion and yield for glycerol oxi-dehydration to acrylic acid for dual and mixed-bed reactor system. Reaction conditions: dehydration catalyst was HZSM-5 (200) and oxidation catalyst was Amor-MoVO; GHSV = 4978 h^{-1}. Conversion and yield data was taken after 3 h time-on-stream.

3.3.4. Effects of crystal structure of MoVO

In the dual bed system, the Amor-MoVO catalyst demonstrated exceptional acrylic acid yield of 67.2 % at 280 °C as shown in Fig. 14 (also shown in Table S6 in the SI). TPR quantitative analysis showed Amor-MoVO having a lower hydrogen uptake capacity compared to Ortho-MoVO (2.562 mmol/g compared to 2.167 mmol/g). Despite this lower reducibility, superior performance suggests that factors such as accessibility to active sites, number of heptagonal channels in the catalyst, and reaction conditions in combination with bed configuration play crucial roles in determining overall catalytic performance. However, as the temperature increased in the dual bed system, acrylic acid yield declined significantly to 48.0 % at 300 °C accompanied by a significant increase in CO_x formation, from 14.3 % at 280 °C to 32.5 % at 300 °C. The formation of acetic acid slightly increased with temperature (14.6 % to 17.4 %), while other by-products like acetaldehyde and propanal were only observed at 260 °C (1.6 % and 1.9 % respectively). For the mixed-bed system, the acrylic acid yield increased with temperature, from 23.0 % at 260 °C to 42.9 % at 300 °C. Moreover, the Amor-MoVO mixed bed system produced significant amounts of acrolein (10.1 % at 260 °C) as well as incomplete glycerol conversion (79.6 %). This indicated that in the mixed bed, the oxidation of acrolein to acrylic acid becomes more efficient at higher temperatures, explaining the increase in acrylic acid yield. The dual bed system showed higher yields of acetic acid (14.6–17.4 %) compared to the mixed bed (1.7–15.3 %). However, the mixed bed produces a more diverse range of by-products, including higher amounts of propanal and others, especially at lower temperatures.

Table 3 presents a comprehensive comparison of glycerol oxi-dehydration to acrylic acid across various molybdenum and vanadium-based catalysts. Comparing the dual bed system having HZSM-5 (200) and MoVO catalyst in the present work clearly demonstrate strong performance, positioning it favourably among the other

Table 3
Conversion and selectivity of oxi-dehydration of glycerol into acrylic acid with different molybdenum and vanadium based heterogeneous catalysts.

Catalyst	Bed type	Temp. (°C)	Feed (N_2 or He/O_2/H_2O/glycerol)	TOS (h)	Conversion (%)	Selectivity (%)	Reference
$FeVO_4$	Single bed	300	66.6/1.7/30.3/1.5	10	100	14	[45]
H_3PO_4/WVNbO	Single bed	285	56/14/25/5	1 to 2	100	59.2	[46]
WVO	Single bed	318	40/4/54/2	2	>99	26	[47]
WVNbO	Single bed	265	42/12/40/6	37	100	50.5	[48]
MoVWO	Single bed	250	41/3/55/1	14	100	30.5	[49]
VO/MFI—zeolite	Single bed	350	27/7/64/2	–	100	17	[50]
Fe/HBEA—zeolite	Single bed	275	74/19/0/7	8	100	23	[51]
MoVO-$H_3PW_{12}O_{40}$/Al_2O_3	Single bed	300	59/4/35/2	2	100	12.1	[52]
$H_{0.1}Cs(VO)_{0.2}(PMo_{12}O_{40})_{0.5}(PW_{12}O_{40})_{0.5}$	Single bed	340	66/4/29/1	1	100	60	[53]
Vanadosilicate	Single bed	320	0/34/64/2	1	93.6	85.4	[54]
$H_4SiW_{12}O_{40}$/Al_2O_3 and MoVO	Dual bed	300	59/4/35/2	2	100	46.2	[52]
$Cs_{2.5}H_{0.5}PW_{12}O_{40}$/$Nb_2O_5$ and SiC-supported-VMo	Dual bed	300	67/12/20/1	24	100	75	[55]
HZSM-5 (200) and MoVO	**Dual bed**	**280**	**58.9/26/33.5/0.7**	**7**	**100**	**67.2**	**This work**

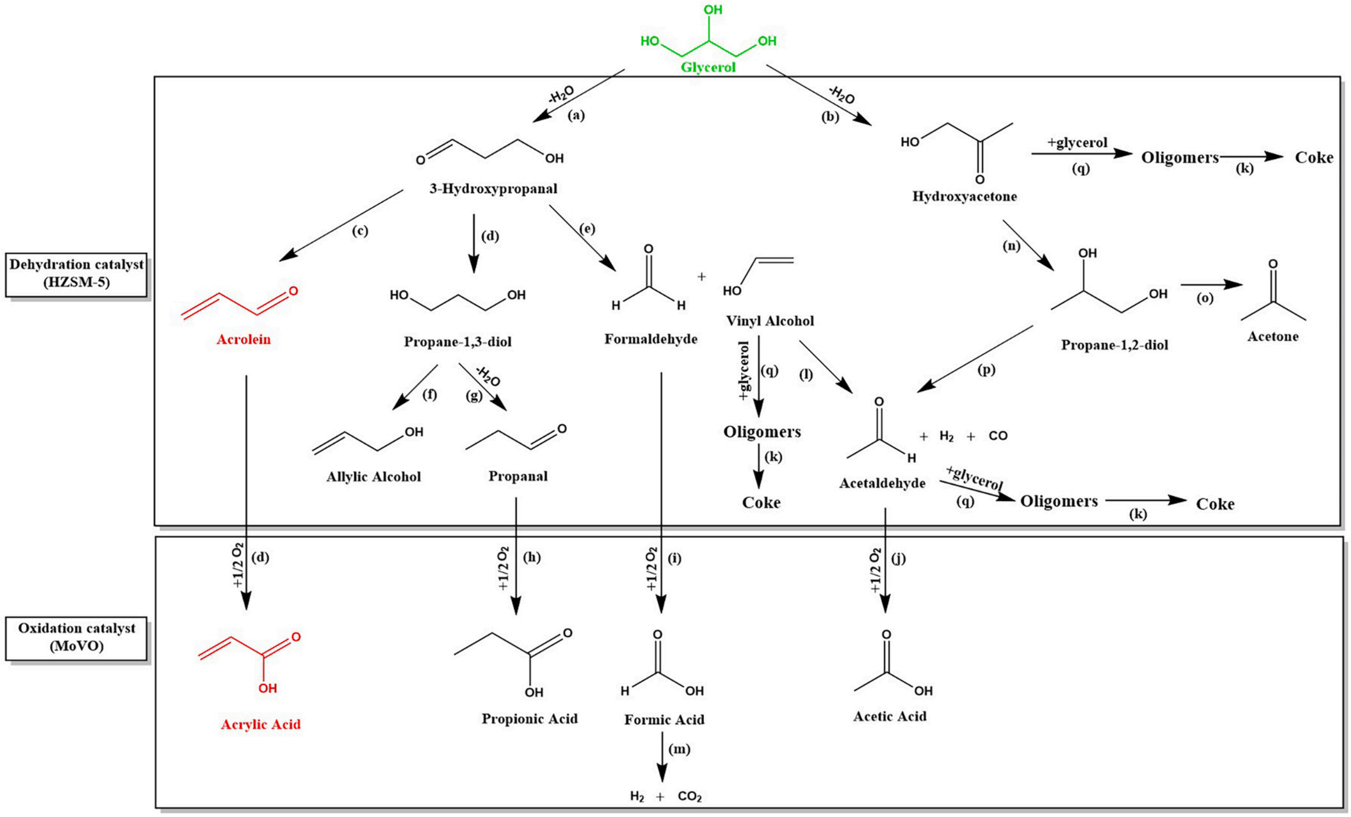

Fig. 15. Modified reaction pathways for glycerol dehydration followed by oxidation.

complex catalyst materials.

3.4. Modified reaction mechanism of glycerol conversion

Fig. 15 proposes the reaction mechanism exhibiting a series of reactions occurring over the dual catalyst system of HZSM-5 and MoVO. The reaction mechanism proposed here has been drawn from the previous literature [15,56–62] and the experimental results obtained in this study both in the presence and absence of oxygen. Moreover, not all the reactions leading to CO_x have been included in this scheme, as almost all the products eventually lead to these compounds. The mechanism can be broadly divided into two main steps: the dehydration of glycerol to acrolein over HZSM-5, and the subsequent oxidation of acrolein to acrylic acid over MoVO. In the first step, glycerol undergoes dehydration on the acidic sites of HZSM-5. The process begins with the protonation of a primary hydroxyl group of glycerol by Brønsted acid sites on the zeolite surface. This is followed by the elimination of a water molecule, leading to the formation of an enol intermediate, 3-hydroxypropanal (a). This unstable intermediate will almost immediately undergo further dehydration to form acrolein (c), which is the primary desired product of this step. However, the presence of Lewis acids on the HZSM-5 catalysts also led to the formation of hydroxyacetone (acetol) (b), which was observed as a byproduct in the experimental results. Similar to 3-hydroxypropanal, 1,2-propanediol was also an intermediate which was not detected, but the presence of acetone (o) and acetaldehyde (p) confirmed its formation. The formation of other by-products, such as formaldehyde and vinyl alcohol, occur through the cleavage of C—C bonds in the glycerol molecule (e). These compounds can further react to form acetaldehyde (l), which was indeed detected in the product mixture. An important aspect of the mechanism is the formation of oligomers (q) and coke (k), which are shown to originate from both glycerol and acetaldehyde. This aligns with the experimental observations of catalyst deactivation due to coke formation, especially in the absence of air.

In the second step of the process, acrolein is oxidized to acrylic acid over the MoVO catalyst (d). This occurs through the adsorption of acrolein on the catalyst surface, followed by the insertion of oxygen from the lattice of the metal oxide. The mechanism shows that this step is relatively straightforward compared to the dehydration step, which explains the high selectivity towards acrylic acid observed in the dual-bed configuration. However, the mechanism also illustrates potential side reactions in this oxidation step ((h), (i) and (j)). Acrolein can be oxidized to propionic acid instead of acrylic acid by first forming propanal through hydrogenation (h), which was indeed observed in the product distribution. The presence of oxygen plays a crucial role in both steps of the reaction. In the dehydration step, oxygen helps to suppress coke formation by oxidizing coke precursors, as evidenced by the increased catalyst stability in the presence of air.

4. Conclusions and future work

This study investigated the continuous chemical process for the catalytic conversion of glycerol to acrylic acid via oxi-dehydration using two different bed configurations. The aim of the research work was to optimize the catalyst design and reaction conditions to maximize acrylic acid yield while minimizing undesired by-products. HZSM-5 zeolites with varying Si/Al ratios were evaluated for the dehydration step, with HZSM-5 (200) emerging as the most promising catalyst due to its balanced properties of high surface area, optimal mesopore volume, and moderate acidity. For the glycerol oxi-dehydration to acrylic acid, the effects of temperature, space velocity, oxygen concentration, and catalyst bed configuration were explored on product distribution. This work demonstrated exceptional acrylic acid yields of up to 67.2 % using a dual-bed configuration with HZSM-5 (200) and Amor-MoVO catalysts at 280 °C and 4972 h^{-1} GHSV - among the highest reported in literature. The use of Ortho-MoVO as the oxidation catalyst in the same configuration achieved 58.8 % acrylic acid yield at optimal conditions (280 °C, 4972 h^{-1} GHSV, glycerol to oxygen ratio of 1:9.5). The superior performance of the dual-bed system can be attributed to the spatial separation of reaction zones, allowing efficient glycerol dehydration without oxygen interference, followed by targeted oxidation of concentrated acrolein stream. While the mixed-bed system offers potential advantages in terms of capital investment through single-reactor operation, the increased formation of by-products (acetaldehyde, propanal, and acrolein) suggests more extensive downstream processing requirements, potentially offsetting the initial economic benefits. The modified reaction mechanism proposed in this work comprehensively explains the interplay of reactions in both dehydration and oxidation steps, providing valuable insights into by-product formation pathways under different reaction conditions. Overall, this research work provides a foundation for developing more efficient and sustainable processes for converting glycerol to high-value acrylic acid. We believe that the insights gained on catalyst design, bed configuration, and reaction conditions, coupled with the demonstrated superior performance of the dual-bed system, will have significant implications for industrial implementation, which will contribute to the much sought-after shift towards a future sustainable chemical industry.

Experiments are currently being scaled up using a 3 cm I.D., 80 cm length reactor to enable a detailed mechanistic study of coke formation pathways. The impact of oxygen distribution via membrane will also be examined. Regeneration studies, will be addressed in future investigations using larger reactor systems, allowing improved spatial resolution.

CRediT authorship contribution statement

Yash Bansod: Writing – review & editing, Writing – original draft, Methodology, Investigation, Formal analysis, Data curation, Conceptualization. **Prashant Pawanipagar:** Writing – review & editing, Validation, Methodology, Investigation, Data curation. **Umar Abubakar:** Writing – review & editing, Investigation, Data curation. **Min Hu:** Writing – review & editing, Validation, Methodology, Investigation, Data curation. **Hassan Alhassawi:** Writing – review & editing, Methodology, Investigation, Data curation. **Kamran Ghasemzadeh:** Writing – review & editing, Methodology, Investigation, Formal analysis, Data curation. **Luke Forster:** Data curation. **Sarayute Chansai:** Resources, Data curation. **Christopher Hardacre:** Resources, Conceptualization. **Vincenzo Spallina:** Writing – review & editing, Validation, Supervision, Resources, Project administration, Investigation, Funding acquisition, Data curation, Conceptualization. **Carmine D'Agostino:** Writing – review & editing, Validation, Supervision, Resources, Project administration, Investigation, Funding acquisition, Data curation, Conceptualization.

Declaration of competing interest

The authors declare that they have no known competing financial interests or personal relationships that could have appeared to influence the work reported in this paper.

Acknowledgements

The authors acknowledge the financial support from the EPSRC "Sustainable Production of ACrylic acId from reNewable waste Glycerol" project, EP/V026089/1. Yash Bansod and Prashant Pawanipagar would like to acknowledge the Social Welfare Department, Government of Maharashtra, India.

Appendix A. Supplementary data

Supplementary data to this article can be found online at https://doi.org/10.1016/j.cej.2025.167723.

Data availability

Data will be made available on request.

References

[1] OECD-FAO Agricultural Outlook 2024–2031, OECD, 2024.
[2] T. Attarbachi, M.D. Kingsley, V. Spallina, Fuel 340 (2023) 127485.
[3] Y. Bansod, B. Crabbe, L. Forster, K. Ghasemzadeh, C. D'Agostino, J. Clean. Prod. 437 (2024) 140485.
[4] A. Sandid, V. Spallina, J. Esteban, Fuel Process. Technol. 253 (2024) 108008.
[5] A. Sandid, J. Esteban, C. D'Agostino, V. Spallina, J. Clean. Prod. 418 (2023) 138127.
[6] D. Arntz, A. Fischer, M. Höpp, S. Jacobi, J. Sauer, T. Ohara, T. Sato, N. Shimizu, H. Schwind, Ullmann's Encyclopedia of Industrial Chemistry, 2007.
[7] U.C. Abubakar, Y. Bansod, L. Forster, V. Spallina, C. D'Agostino, React. Chem. Eng. 8 (2023) 1819–1838.
[8] S.H. Chai, H.P. Wang, Y. Liang, B.Q. Xu, Appl. Catal. Gen. 353 (2009) 213–222.
[9] E. Tsukuda, S. Sato, R. Takahashi, T. Sodesawa, Catal. Commun. 8 (2007) 1349–1353.
[10] B. Ali, X. Lan, M.T. Arslan, S.Z.A. Gilani, H. Wang, T. Wang, J. Ind. Eng. Chem. 88 (2020) 127–136.
[11] Z. Wang, L. Wang, Y. Jiang, M. Hunger, J. Huang, ACS Catal. 4 (2014) 1144–1147.
[12] M. Herbon, A. Lange, M. Weiß, W. Suprun, D. Enke, Chem. Eng. Technol. 38 (2015) 431–440.
[13] A. Ulgen, W. Hoelderich, Catal letters 131 (2009) 122–128.
[14] T.M. Neves, J.O. Fernandes, L.M. Lião, E. Deise da Silva, C. Augusto da Rosa, V. B. Mortola, Microporous and Mesoporous Materials 275 (2019) 244–252.
[15] A. Witsuthammakul, T. Sooknoi, Appl. Catal. Gen. 413–414 (2012) 109–116.
[16] L.G. Possato, W.H. Cassinelli, T. Garetto, S.H. Pulcinelli, C.V. Santilli, L. Martins, Appl. Catal. Gen. 492 (2015) 243–251.
[17] P. Lauriol-Garbey, G. Postole, S. Loridant, A. Auroux, V. Belliere-Baca, P. Rey, J.M. M. Millet, Appl. Catal. B. 106 (2011) 94–102.

[18] X.C. Jiang, C.H. Zhou, R. Tesser, M. Di Serio, D.S. Tong, J.R. Zhang, Ind. Eng. Chem. Res. 57 (2018) 10736–10753.
[19] Y. Bansod, P. Pawanipagar, K. Ghasemzadeh, C. D'Agostino, Green Chem. 26 (2024) 9840–9858.
[20] S. Ishikawa, W. Ueda, Crystalline Metal Oxide Catalysts (2022) 101–121.
[21] C. Chen, N. Kosuke, T. Murayama, W. Ueda, ChemCatChem 5 (2013) 2869–2873.
[22] Y.S. Yun, K.R. Lee, H. Park, T.Y. Kim, D. Yun, J.W. Han, J. Yi, ACS Catal. 5 (2015) 82–94.
[23] P. Morales-Pacheco, J.M. Domínguez, L. Bucio, F. Alvarez, U. Sedran, M. Falco, Catal. Today 166 (2011) 25–38.
[24] A.L. Patterson, Phys. Rev. 56 (1939) 978.
[25] T. Katou, D. Vitry, W. Ueda, Catal today 91–92 (2004) 237–240.
[26] S. Narayanan, J.J. Vijaya, S. Sivasanker, C. Ragupathi, T.M. Sankaranarayanan, L. J. Kennedy, J. Porous. Mater. 23 (2016) 741–752.
[27] Y.P. Guo, H.J. Wang, Y.J. Guo, L.H. Guo, L.F. Chu, C.X. Guo, Chem. Eng. J. 166 (2011) 391–400.
[28] Y. Fang, H. Hu, J. Am. Chem. Soc. 128 (2006) 10636–10637.
[29] P. Botella, P. Concepción, J.M. López Nieto, B. Solsona, Catal. Letters 89 (2003) 249–253.
[30] P. Botella, B. Solsona, A. Martinez-Arias, J.M. López Nieto, Catal. Letters 74 (2001) 149–154.
[31] S. Ishikawa, T. Murayama, S. Ohmura, M. Sadakane, W. Ueda, Chem. Mater. 25 (2013) 2211–2219.
[32] M. Thommes, K. Kaneko, A.V. Neimark, J.P. Olivier, F. Rodriguez-Reinoso, J. Rouquerol, K.S.W. Sing, Pure Appl. Chem. 87 (2015) 1051–1069.
[33] L. Huang, F. Qin, Z. Huang, Y. Zhuang, J. Ma, H. Xu, W. Shen, Ind. Eng. Chem. Res. 55 (2016) 7318–7327.
[34] F. Lónyi, J. Valyon, Microporous Mesoporous Mater. 47 (2001) 293–301.
[35] N. Robinson, P. Bräuer, A.P.E. York, C. D'Agostino, Phys. Chem. Chem. Phys. 23 (2021) 17752–17760.
[36] B.S. Liu, Y. Zhang, J.F. Liu, M. Tian, F.M. Zhang, C.T. Au, A.S.C. Cheung, J. Phys. Chem. C 115 (2011) 16954–16962.
[37] P. He, R. Gatip, M. Yung, H. Zeng, H. Song, Appl Catal B 211 (2017) 275–288.
[38] B.O. Dalla Costa, M.A. Peralta, C.A. Querini, Appl. Catal. Gen. 472 (2014) 53–63.
[39] Y.T. Kim, K.D. Jung, E.D. Park, Appl. Catal. Gen. 393 (2011) 275–287.
[40] J.O. Fernandes, T.M. Neves, E.D. da Silva, C.A. da Rosa, V.B. Mortola, Reaction Kinetics, Mechanisms and Catalysis 132, 2021, pp. 485–498.
[41] T.M. Neves, J.O. Fernandes, L.M. Lião, E. Deise da Silva, C. Augusto da Rosa, V. B. Mortola, Microporous and Mesoporous Materials 275 (2019) 244–252.
[42] G.L. Catuzo, L.G. Possato, M.E. Sad, C. Padró, L. Martins, ChemCatChem 13 (2021) 4419–4430.
[43] T. Fjermestad, W. qing Li, G. Rugg, S. Ishida, M. Okuno, K. Sagi, A. Genest, N. Rösch, Appl. Catal. Gen. 565 (2018) 68–75.
[44] T.V. Andrushkevich, Catalysis Reviews—Science and Engineering 35, 1993, pp. 213–259.
[45] F. Wang, J. Xu, J.L. Dubois, W. Ueda, ChemSusChem 3 (2010) 1383–1389.
[46] K. Omata, K. Matsumoto, T. Murayama, W. Ueda, Catal. Today 259 (2016) 205–212.
[47] M.D. Soriano, P. Concepción, J.M.L. Nieto, F. Cavani, S. Guidetti, C. Trevisanut, Green Chem. 13 (2011) 2954–2962.
[48] A. Chieregato, M.D. Soriano, F. Basile, G. Liosi, S. Zamora, P. Concepción, F. Cavani, J.M. López Nieto, Appl. Catal. B 150–151 (2014) 37–46.
[49] Y.S. Yun, K.R. Lee, H. Park, T.Y. Kim, D. Yun, J.W. Han, J. Yi, ACS Catal. 5 (2015) 82–94.
[50] L.G. Possato, W.H. Cassinelli, T. Garetto, S.H. Pulcinelli, C.V. Santilli, L. Martins, Appl. Catal. A. Gen. 492 (2015) 243–251.
[51] M.M. Diallo, J. Mijoin, S. Laforge, Y. Pouilloux, Catal. Commun. 79 (2016) 58–62.
[52] L. Liu, B. Wang, Y. Du, Z. Zhong, A. Borgna, Appl. Catal. B-Environ. Energy 174–175 (2015) 1–12.
[53] X. Li, Y. Zhang, ACS Catal. 6 (2016) 2785–2791.
[54] A.S. Paula, L.G. Possato, D.R. Ratero, J. Contro, K. Keinan-Adamsky, R.R. Soares, G. Goobes, L. Martins, J.G. Nery, Micropor. Mesopor. Mat. 232 (2016) 151–160.
[55] R. Liu, T. Wang, D. Cai, Y. Jin, Ind. Eng. Chem. Res. 53 (2014) 8667–8674.
[56] I. Martinuzzi, Y. Azizi, J.F. Devaux, S. Tretjak, O. Zahraa, J.P. Leclerc, Chem. Eng. Sci. 116 (2014) 118–127.
[57] F. Wang, J.L. Dubois, W. Ueda, J. Catal. 268 (2009) 260–267.
[58] E. Tsukuda, S. Sato, R. Takahashi, T. Sodesawa, Catal. Commun. 8 (2007) 1349–1353.
[59] W. Suprun, M. Lutecki, T. Haber, H. Papp, J. Mol. Catal. A Chem. 309 (2009) 71–78.
[60] A. Corma, G.W. Huber, L. Sauvanaud, P. O'Connor, J. Catal. 257 (2008) 163–171.
[61] S.H. Chai, H.P. Wang, Y. Liang, B.Q. Xu, Green Chem. 9 (2007) 1130–1136.
[62] J. Deleplanque, J.L. Dubois, J.F. Devaux, W. Ueda, Catal. Today 157 (2010) 351–358.